

Surface Acoustic Wave Devices Using Lithium Niobate on Silicon Carbide

Shibin Zhang¹, Member, IEEE, Ruochen Lu², Member, IEEE, Hongyan Zhou,
Steffen Link, Student Member, IEEE, Yansong Yang³, Member, IEEE, Zhongxu Li,
Kai Huang, Xin Ou, and Songbin Gong⁴, Senior Member, IEEE

Abstract—This work demonstrates a group of shear horizontal (SH0) mode resonators and filters using lithium niobate (LiNbO₃) thin films on silicon carbide (SiC). The single-crystalline X-cut LiNbO₃ thin films on 4H-SiC substrates have been prepared by ion-slicing and wafer-bonding processes. The fabricated resonator has demonstrated a large effective electromechanical coupling (k^2) of 26.9% and a high-quality factor (Bode- Q) of 1228, hence resulting in a high figure of merit (FoM = $k^2 \cdot \text{Bode-}Q$) of 330 at 2.28 GHz. Additionally, these fabricated resonators show scalable resonances from 1.61 to 3.05 GHz and impedance ratios between 53.2 and 74.7 dB. Filters based on demonstrated resonators have been demonstrated at 2.16 and 2.29 GHz with sharp roll-off and spurious-free responses over a wide frequency range. The filter with a center frequency of 2.29 GHz shows a 3-dB fractional bandwidth of 9.9%, an insertion loss of 1.38 dB, an out-of-band rejection of 41.6 dB, and a footprint of 0.75 mm². Besides, the fabricated filters also show a temperature coefficient of frequency of -48.2 ppm/°C and power handling of 25 dBm. Although the power handling is limited by arc discharge and migration-induced damage of the interdigital electrodes and some ripples in insertion loss and group delay responses are still present due to the transverse spurious modes, the demonstrations

still show that acoustic devices on the LiNbO₃-on-SiC platform have great potential for radio-frequency applications.

Index Terms—Figure of merit (FoM), impedance ratio, lithium niobate, MEMS, piezoelectric filters, piezoelectric resonators, power handling, shear horizontal (SH0) modes, silicon carbide, temperature of frequency (TCF).

I. INTRODUCTION

RADIO-FREQUENCY acoustic devices are an essential part of the front ends for emerging applications in 5G and IoT. While RF acoustic devices have experienced tremendous market growth in the past decade due to the increasing number of bands incorporated for LTE and global compatibilities, developments and advances in these devices are ever accelerating in anticipation of the wider bandwidth and higher frequency requirements of the future generations. One of the most exciting advances in recent years is the acoustic devices based on transferred lithium niobate thin films, which were first enabled by the ion slicing technique developed for integrated photonics in the 90s [1]. These LiNbO₃ thin-film devices so far have taken various forms (suspended [2] or solidly mounted [3]) and employed a diversity of modes (SAW [4], shear horizontal (SH0) [5], [6], S0 [7], [8], and A1 [9], [10]) over a wide range of frequencies from kHz to 30 GHz. They all have their unique merits and can be compared and rationalized based on how one categorizes them. For instance, the devices that use free-standing LiNbO₃ thin films typically can achieve more significant electromechanical coupling and higher quality factors. However, the latter is still debatable as Q depends on the design as well as fabrication in an interleaved and complex fashion. On the other hand, solidly mounted or unreleased LiNbO₃ devices [3], [11], [12] can feature a more straightforward process, lower cost, larger power handling, and better linearity. In terms of the material stacks for both types of devices, they typically use a transferred LiNbO₃ thin film on either a LiNbO₃ or Si substrate, occasionally with an intermediate layer of SiO₂ for film transfer, device release, or temperature compensation purpose.

For unreleased devices, Si substrates are also typically chosen so far as they are low cost and can support confined propagation of SAW predominantly in LiNbO₃ due to the sharp contrast of material properties between Si and LiNbO₃ and their implied dispersions. Record high performance has been reported as a result of the optimal exploitation of such a material stack. To further advance the performance while taking a similar material-driven approach, it is natural to pose the question if Si is the best substrate available for engineering

Manuscript received January 31, 2020; revised May 4, 2020; accepted May 18, 2020. Date of publication July 13, 2020; date of current version September 2, 2020. This work was supported in part by the College of Engineering, University of Illinois at Urbana Champaign, in part by the National Natural Science Foundation of China under Grant 61851406, in part by the Frontier Science Key Program of CAS under Grant QYZDY-SSW-JSC032, in part by the Chinese–Austrian Cooperative Research and Development Project under Grant GJHZ201950, in part by the K.C.Wong Education Foundation under Grant GJTD-2019-11, and in part by the China Scholarship Council (CSC) under Grant 201804910765. (Corresponding author: Shibin Zhang.)

Shibin Zhang was with the State Key Laboratory of Functional Materials for Informatics, Shanghai Institute of Microsystem and Information Technology, Shanghai 200050, China, and also with the Department of Electrical and Computing Engineering, University of Illinois at Urbana–Champaign, Urbana, IL 61801 USA. He is now with the Center of Materials Science and Optoelectronics Engineering, University of Chinese Academy of Sciences, Beijing 100049, China (e-mail: sbzhang@mail.sim.ac.cn).

Ruochen Lu, Steffen Link, Yansong Yang, and Songbin Gong are with the Department of Electrical and Computing Engineering, University of Illinois at Urbana–Champaign, Urbana, IL 61801 USA (e-mail: songbin@illinois.edu).

Hongyan Zhou and Zhongxu Li are with the State Key Laboratory of Functional Materials for Informatics, Shanghai Institute of Microsystem and Information Technology, Chinese Academy of Sciences, Shanghai 200050, China, and also with the Center of Materials Science and Optoelectronics Engineering, University of Chinese Academy of Sciences, Beijing 100049, China.

Kai Huang and Xin Ou are with the State Key Laboratory of Functional Materials for Informatics, Shanghai Institute of Microsystem and Information Technology, Chinese Academy of Sciences, Shanghai 200050, China (e-mail: ouxin@mail.sim.ac.cn).

Color versions of one or more of the figures in this article are available online at <http://ieeexplore.ieee.org>.

Digital Object Identifier 10.1109/TMTT.2020.3006294

such devices; if not, then what material is better and what modes it can support confined propagation. Without considering the cost and the availability of the substrate, diamond is the best material [13], [14]. However, for implementing deployable devices, diamond might be slightly out of reach although future development on diamond thin film synthesis on Si might help to reduce the cost and widen the access. Excluding diamond, the next best material is silicon carbide (SiC) as it has a desirable mix of properties with respect to LiNbO₃. The large phase velocities for the longitudinal (12 500 m/s) and shear waves (7100 m/s) [15], the exceptionally high thermal conductivity [370 W/(m·K)] [16], the Si-comparable but much lower than LiNbO₃ dielectric constant, and the great $f \cdot Q$ product all promise great device performance and possibly a new type of devices for harsh environment applications for which SiC is also known.

To explore the potential of the LiNbO₃ on 4H-SiC Platform, this work designs and demonstrates the first class of high-performance RF acoustic resonators and filters on such a platform prepared by ion-slicing and wafer-bonding processes. The fabricated resonators with effective electromechanical coupling coefficients greater than 20% show scalable resonances from 1.61 to 3.05 GHz, and impedance ratios between 53.2 and 74.7 dB. Filters with the same topology have been demonstrated at 2.16 and 2.29 GHz with sharp roll-off and spurious-free response over a wide frequency range. The filter with a center frequency of 2.29 GHz shows the excellent bandwidth, the good out-of-band rejection, and the decent IL. Besides, the temperature of frequency (TCF) and power handling of the filter have also been studied.

The rest of this article is organized as follows. Section II offers the design of RF acoustic resonators and filters on the LiNbO₃-on-SiC platform. Section III presents the fabricated LiNbO₃ thin film on SiC and the SH₀ resonators and filters. Section IV presents and discusses the measured results of the resonators and the filters, including the admittance responses of the resonators, S-parameters, TCF, and power handling of the filters. Finally, the conclusion is stated in Section V.

II. DEVICE DESIGN

A. SAW Resonators on Heterointegrated Substrates

The schematic of a typical one-port SAW resonator on a heterointegrated substrate is shown in Fig. 1 with the key parameters explained in Table I. The top view of the resonator is shown in Fig. 1(a), where two grating reflectors are placed at both ends of the interdigital transducers (IDTs). The IDTs are composed of N_i pairs of metal strips aligned and connected to the busbars periodically, while the grating reflectors are composed of N_r pairs of shorted metal strips. The period P_r of the grating reflectors is generally set to half of P_i so that the resonant frequencies of the IDT and the reflectors align with each other and desired mechanical reflection can be achieved [17]. The cross-sectional view of the resonator is shown in Fig. 1(b), where the single-crystal LiNbO₃ thin film is transferred onto a substrate. Although the performance of this kind of SAW resonators will be affected by a variety of factors, such as its mode of operation, dispersion,

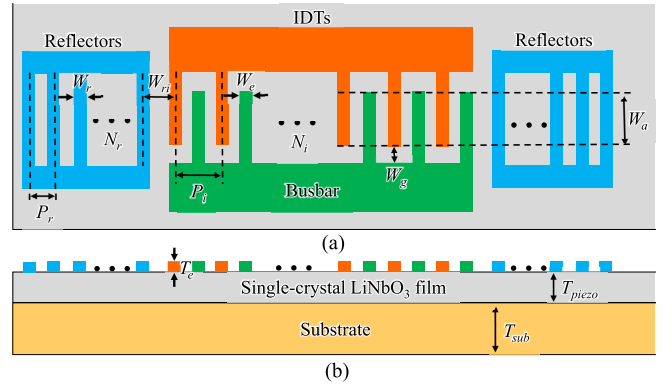


Fig. 1. Schematic of a one-port resonator with key design parameters. (a) Top view. (b) Cross-sectional view.

TABLE I
KEY PARAMETERS OF SOLIDLY MOUNTED RESONATORS

Sym.	Parameter	Sym.	Parameter
T_{piezo}	Piezoelectric film thickness	W_e	IDT finger width
T_{sub}	Substrate thickness	W_r	Reflector finger width
T_e	Electrode thickness	W_a	Aperture width
P_i	IDT finger period	W_g	Air gap width
P_r	Reflector finger period	W_{ri}	Air gap width
N_i	Number of IDT pairs	N_r	Number of reflector pairs

electrode configuration, the material properties of the selected substrate, and a variety of device design details, the selected substrate plays a fundamental role in determining the mode that can be excited and confined, as well as the quality factor, electromechanical coupling, thermal and power handling of the device.

B. Comparison of Different Substrates

Since the substrate is so important, it is beneficial first to analyze the causality between material properties and device performance in a general and device-design-agnostic fashion and subsequently establish the following criteria and their rationale:

- 1) large phase velocity contrast to LiNbO₃, i.e., a harder material with lower density;
- 2) large thermal conductivity and capacity for better power handling and wider temperature range of operation;
- 3) low mismatch in coefficient of thermal expansion for bonding robustness over a wide temperature range;
- 4) significant lower dielectric constants than that of LiNbO₃ for electrical field confinement in LiNbO₃;
- 5) low acoustic loss and large intrinsic $f \cdot Q$ product so that if any acoustic fields are present in the substrate material, propagation in the substrate will not induce high loss;
- 6) not prohibitively expensive.

Note that the above criteria are qualitative and do not strictly predict device performance superiority. However, it is

TABLE II
MATERIAL PROPERTIES OF DIFFERENT SUBSTRATES

Substrates	Density (kg/m ³)	Stiffness constants (GPa)	v_l (m/s)	v_s (m/s)	Relative permittivity	Thermal conductivity (W/(m·K))	Thermal expansion (ppm/°C)	Cost	Reference
<i>LiNbO₃</i>	4628	$C_{11}=198, C_{44}=59.7$	6541	3592	{45.6, 45.6, 26.3}	4.2	{14.4, 15.9, 7.5}	Low	[18], [19], [20]
<i>Silicon</i>	2329	$C_{11}=166, C_{66}=79.6$	8442	5846	11.7	142	2.6	Very low	[21], [22], [23]
<i>3C-SiC (Polycrystalline)</i>	3210	$C_{11}=371, C_{66}=111$	10751	5880	10.5	64	4.1	Low	[24], [25], [26], [27]
<i>3C-SiC</i>	3210	$C_{11}=352, C_{66}=232$	10472	8501	9.7	360	3.8	Medium	[28], [16]
<i>4H-SiC</i>	3210	$C_{11}=501, C_{44}=163$	12493	7126	{9.7, 10.0}	370	{3.1, 3.2}	Medium	[15], [16], [29]
<i>6H-SiC</i>	3210	$C_{11}=501, C_{44}=163$	12493	7126	{9.7, 10.0}	490	{3.2, 3.3}	Medium	[15], [16], [29]
<i>Diamond</i>	3515	$C_{11}=1079, C_{66}=578$	17521	12823	5.9	600-2000	1.1	High	[13], [30], [14], [31]
<i>Sapphire (α-Al₂O₃)</i>	3968	$C_{11}=490, C_{44}=145$	11113	6045	{9.4, 11.5}	32.5	{5.0, 6.6}	Low	[32], [33]
<i>α-quartz</i>	2649	$C_{11}=86.7, C_{44}=57.9$	5721	4675	{3.9, 4.1}	11.1	{13.7, 7.5}	Low	[34], [35], [36]
<i>SiO₂ (Amorphous)</i>	2200	$C_{11}=75.0, C_{44}=22.5$	5839	3198	3.5	1.1-1.4	0.6	Low	[37], [38]

still valuable to compare available materials based on these criteria in the material selection process. To this end, we collect the material properties of some commercially available substrates in Table II for comparison [13]–[16], [18]–[38]. The propagation characteristics of longitudinal and shear waves in different crystal materials are derived and explained in detail in [39] and [40]. Although the propagation of bulk waves in anisotropic elastic materials is quite complicated, we are most concerned about the phase velocities of the slow shear wave (v_s) and the slow longitudinal wave (v_l). Here, the slow longitudinal wave refers to the longitudinal wave with the slowest phase velocity in an anisotropic elastic material. For hexagonal (e.g., 4H-SiC, 6H-SiC) and trigonal (e.g., LiNbO₃, Sapphire, α-quartz) materials, the corresponding phase velocities can be approximated by [39], [40]

$$v_l \approx \sqrt{c_{11}/\rho} \quad (1)$$

$$v_s \approx \sqrt{c_{44}/\rho} \quad (2)$$

while for cubic (e.g., silicon, 3C-SiC, diamond) materials, the corresponding velocities can be approximated by [39]

$$v_l \approx \sqrt{c_{11}/\rho} \quad (3)$$

$$v_s \approx \sqrt{c_{66}/\rho} \quad (4)$$

where c_{11} and c_{44} (c_{66}) are stiffness constants related to the longitudinal and shear waves, respectively, and ρ is the material density.

Let us consider a typical device structure in Fig. 1 and suppose that the LiNbO₃ thin films are transferred to the heterogeneous substrates listed in Table II. The electrical energy confinement of the intended mode in the thickness direction will be related to the dielectric constants of the selected substrate, and lower dielectric constant provides a higher electromechanical coupling. Besides, the mechanical energy confinement is closely related to the phase velocities

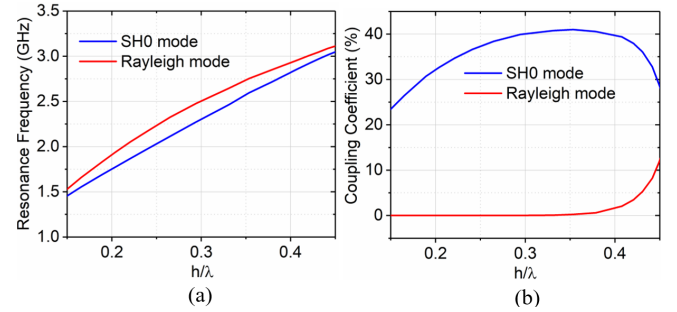


Fig. 2. Simulated dispersion curves of the SH0 and Rayleigh modes in a transducer cell in an X-cut LiNbO₃ thin film on a 4H-SiC substrate. (a) Resonant frequency versus h/λ . (b) Coupling coefficient k^2 versus h/λ .

of the shear and the longitudinal bulk waves in the selected substrate. Larger phase velocity contrast to the intended mode will provide better energy confinement. It is probably not surprising that diamond is the best material although it might be too costly for making deployable devices. The next best material is SiC, as it has the desirable mix of properties with respect to LiNbO₃. Among the various types of SiC, 4-H and 6-H are preferred due to the large thermal conductivities and availability.

C. SH0 Mode Resonators in LiNbO₃ on SiC

Considering a hetero-integrated X-cut LiNbO₃ thin film on 4H-SiC, the simulated dispersion curves of the SH0 mode and Rayleigh mode in a transducer cell are presented in Fig. 2, where h is the thickness of the transferred LiNbO₃ thin film, and λ is the wavelength of the excited SH0 (Rayleigh) mode. k^2 of SH0 waves versus the propagation direction in the X-cut LiNbO₃ plate has been studied in [41], [42]. The maximum k^2 orientation is around -10° to the $+Y$ -axis. To suppress Rayleigh waves while attaining large k^2 , the propagation

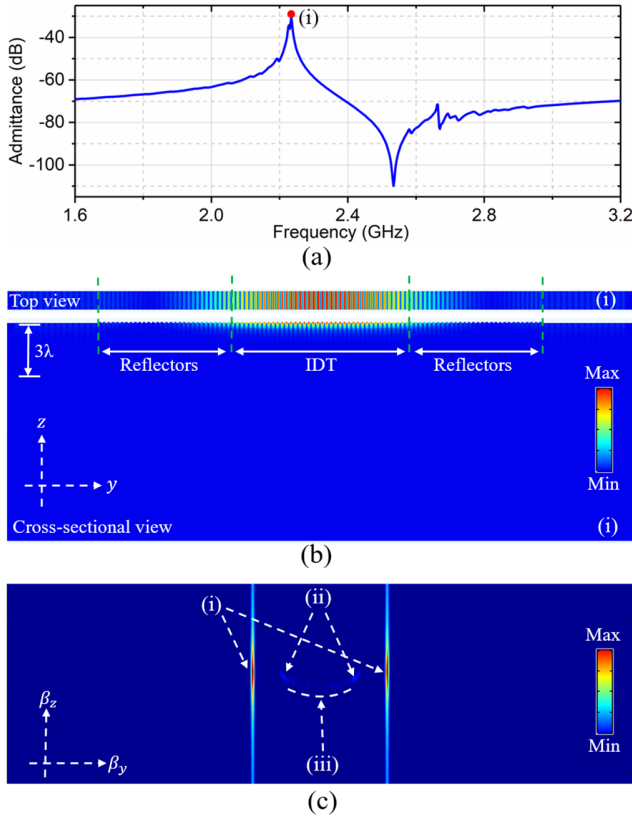


Fig. 3. (a) Simulated admittance response of a one-port SH0 mode resonator. (b) Top view and the cross-sectional view of the displacement mode shapes at the resonant frequency in the real-space domain (y - z). (c) Cross-sectional view of the displacement mode shapes at the resonant frequency in the wavenumber domain ($\beta_y - \beta_z$).

direction is set to -12° to the $+Y$ -axis. As shown in Fig. 2(a), when h/λ is between 0.15 and 0.45, the resonant frequency of the intended SH0 mode is always lower than that of the Rayleigh mode, which means that the Rayleigh mode shows up as in-band spurious mode. Note that the phase velocity of the intended SH0 mode is dispersive and is related to the ratio of h/λ , which determines the effective stiffness of the LiNbO₃ thin film. When h/λ is between 0.15 and 0.35, the corresponding coupling coefficient of the intended SH0 mode gradually increases while that of the Rayleigh mode is almost 0. When h/λ is between 0.35 and 0.45, the coupling coefficient of the intended SH0 mode gradually decreases while that of the Rayleigh mode gradually increases to 12%, as shown in Fig. 2(b). Therefore, to mitigate the effect of the in-band Rayleigh mode of an SH0 mode resonator, h/λ should be set to be less than 0.35.

Following the guideline above, we set the operating wavelength λ is $1.86 \mu\text{m}$, and the thickness of the LiNbO₃ and the SiC substrate is 530 nm and $500 \mu\text{m}$, respectively. We then design an SH0 mode resonator with 20 pairs of IDTs and 15 pairs of reflectors on the opposite ends of the IDTs on the LiNbO₃-on-SiC substrate. The resonator is simulated with 3-D finite element analysis (FEA) in COMSOL Multiphysics. As shown in Fig. 3(a), the simulation indicates a resonance of 2.234 GHz and a k^2 of 35.3% for the intended SH0 mode.

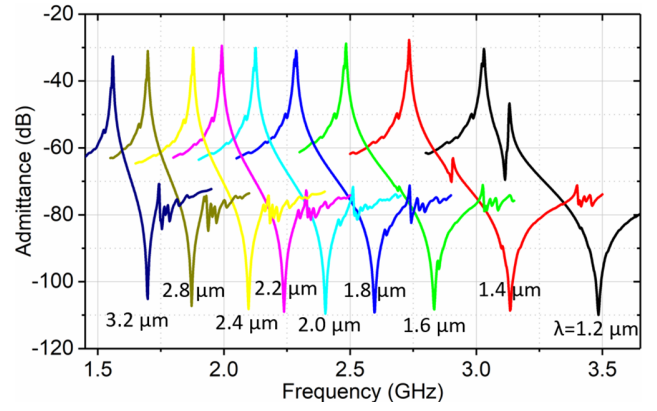


Fig. 4. Simulated admittance responses of SH0-mode resonators at different wavelengths.

k^2 is given by $k^2 = \pi^2/8 \times (f_p^2 - f_s^2)/f_s^2$, where f_s and f_p are resonant and antiresonant frequencies, respectively. The top view and the cross-sectional view of the displacement mode shapes of the intended SH0 mode in the real-space domain (y - z) are shown in Fig. 3(b), from which we can find the energy of the SH0 mode is well confined in the surface (LiNbO₃ film) of the LiNbO₃-on-SiC substrate. In addition, as shown in Fig. 3(c), the displacement vectors (obtained from the FEA) in the real-space domain (y - z) are converted into the wavenumber domain ($\beta_y - \beta_z$) using a calculation method of 2-D fast Fourier transform (2D-FFT) indicated in [43]. The wavenumber domain is equivalent to a spatial frequency spectrum, where the separation of acoustic wave modes can be visualized, and the characteristics and the relations between the modes can be analyzed. In the wavenumber domain depicted in Fig. 3(c), two lines stretch in the z -direction with long red areas (i), which correspond to the SH0-SAW traveling in the surface area in Fig. 3(b). In the center of Fig. 3(c), lighter blue curves of the shear bulk wave responses (iii) and the longitudinal bulk wave responses (ii) in the SiC substrate can be seen in the dark blue backdrop [39]. Note that the light blue curves representing the shear (iii) and the longitudinal (ii) waves in the SiC substrate do not contact that of the SH0-SAW (i). This is due to the large contrast of the phase velocities between (i) and (ii) as well as between (i) and (iii), and the SH0-SAW can only be converted into the shear or the longitudinal waves in the SiC substrate with a large radiation angle. Therefore, hardly any bulk wave radiation is generated and that the energy of the SH0-SAW can be maintained in the surface area.

Fig. 4 shows the simulated admittance responses of the SH0-mode resonators that share a similar device structure to the resonator in Fig. 3(b) at different wavelengths. When $\lambda = 1.2$ and $1.4 \mu\text{m}$ (the corresponding $h/\lambda = 0.442, 0.378$), the in-band Rayleigh mode is strong and the main resonance response of the SH0 mode is notably affected, which is consistent with the simulation results shown in Fig. 2.

D. Acoustic Filters

In this section, a high-order ladder-type filter consisting of series and shunt resonators is designed. The resonant

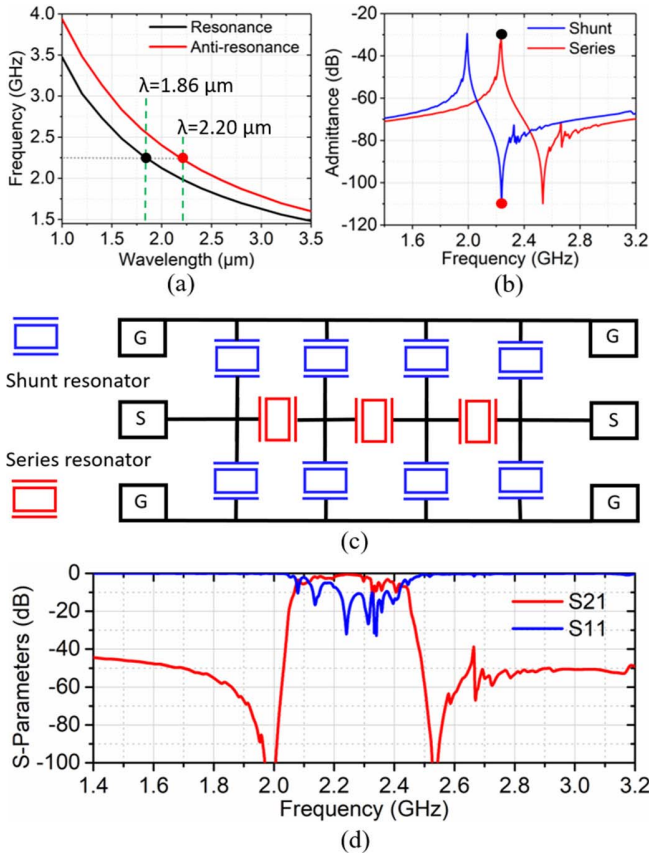


Fig. 5. (a) Simulated dispersion curves of the SH0 mode in a 530 nm thick X-cut LiNbO₃ thin film on a 4H-SiC substrate. (b) Simulated admittance responses of the series and shunt resonators. (c) Topology of a high-order ladder-type filter. (d) Simulated S-parameters (S_{11} and S_{21}) of the high-order ladder-type filter.

frequencies of series and shunt resonators are designed with a frequency offset between them, which approximately gives the bandwidth of the filter [44]. To achieve a large bandwidth allowed by the k^2 of these standalone resonators, the offset should approach the spectral separation between the resonances and the antiresonances. The required frequency offset can be attained by varying the period of the IDT fingers (P_i or λ) as suggested by the dispersion curves of SH0 mode shown in Fig. 5(a). This technique permits the monolithic implementation of multifrequency resonators required by the ladder topology as well as the lithography-based frequency trimming.

Fig. 5(b) shows the simulated admittance responses of the designed series and shunt resonators. The wavelength of the series resonators is set to 1.86 μm for attaining a filter center frequency at 2.23 GHz, while the wavelength of the shunt resonators is set to 2.20 μm for attaining the required frequency offset of 250 MHz and achieving a fractional bandwidth (FBW) greater than 10%. Fig. 5(c) shows the topology of the high-order ladder-type filter. To make the filter footprint compact and symmetric, each shunt branch is implemented with two identical resonators in parallel. To attain an adequate C_0 for matching to 50 Ω and sufficient out-of-band rejection of 40 dB, the numbers of the IDT finger pairs are increased to

TABLE III
KEY PARAMETERS OF SERIES AND SHUNT RESONATORS

Parameter	T_e (nm)	λ (μm)	W_e (nm)	W_a (λ)	N_i (pair)
Series resonator 1#	130	1.86	465	19	44
Series resonator 2#	130	1.86	465	20	44
Series resonator 3#	130	1.86	465	21	44
Shunt resonator	130	2.20	550	22	72

44 and 72, respectively, for series and shunt resonators. Last, to mitigate the effect of the transverse modes, the apertures (W_a) of the series resonators are set to 19λ , 20λ , and 21λ . The key parameters of the series and shunt resonators are listed in Table III. The simulated performance (S_{21}) of the high-order filter is shown in Fig. 5(d), exhibiting an OoB level of about 40 dB.

III. MATERIAL AND DEVICE FABRICATION

A. Fabrication of X-Cut LiNbO₃ Thin Films on SiC Substrates

The heterogeneous integration of a single-crystalline LiNbO₃ thin film onto a 4H-SiC substrate is achieved by the ion-slicing process [1], [45]. First, a 4-in LiNbO₃ wafer is implanted with helium ions (He⁺) at a 7° tilt to minimize the ion channeling effect. Then, wafer bonding is performed at 100 °C. The bonded wafer pair subsequently underwent an annealing process so that the implanted He⁺ migrated to induce the exfoliation of the LiNbO₃ thin film. A 4-in LiNbO₃ thin film with a thickness of less than 600 nm is eventually split from the bulk wafer and transferred on the SiC substrate. Finally, the rough and exfoliated surface is smoothed with inductively coupled plasma (ICP) etching.

Fig. 6(a) presents a cross-sectional transmission electron microscope (XTEM) image of the fabricated LiNbO₃-on-SiC sample, in which the glue is used to increase the conductivity of the sample surface to assist the preparation of the TEM sample. The bonding interface between the LiNbO₃ film and the SiC substrate was investigated by high-resolution TEM (HRTEM), as shown in Fig. 6(b). A 3.7-nm amorphous SiO₂ layer at the bonding interface was formed due to the surface oxidation of the SiC. Furthermore, the selected area electron diffraction (SAED) pattern of the transferred LiNbO₃ in the inset of Fig. 6(b) suggests the high crystallinity of the transferred LiNbO₃ thin film, too. Fig. 6(c) presents the atomic force microscope (AFM) image of the transferred LiNbO₃-on-SiC sample, and the uniform root-mean-square (rms) roughness value less than 2 nm is obtained after ICP etching. The full-width at half-maximum (FWHM) of the XRD rocking curve of the transferred LiNbO₃ after ICP etching is 122 arcsec, again confirming the high crystallinity of the LiNbO₃ thin film.

B. Fabrication of the Devices

The devices were in-house fabricated. First, the device patterns were formed by electron beam lithography, aluminum

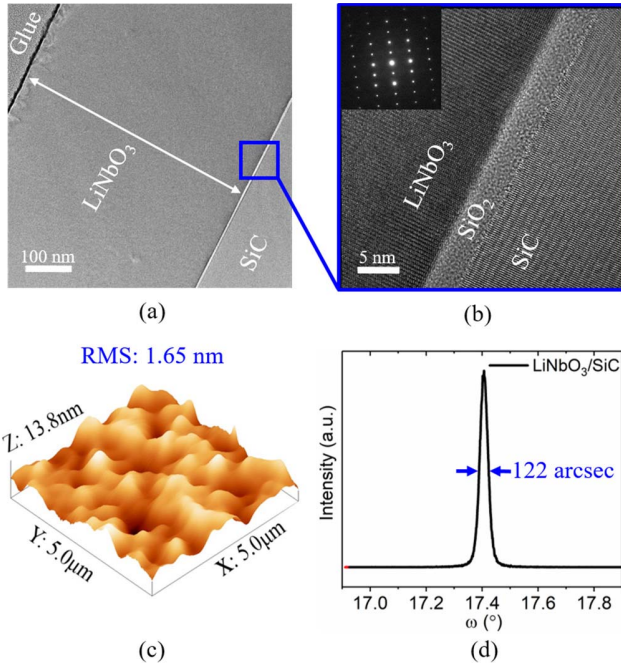


Fig. 6. (a) XTEM image and (b) HRTEM image of a single-crystalline LiNbO_3 thin film on a 4H-SiC substrate. (c) AFM image of the transferred LiNbO_3 thin film after ICP etching. (d) XRD rocking curve for (110) plane of the transferred LiNbO_3 thin film.

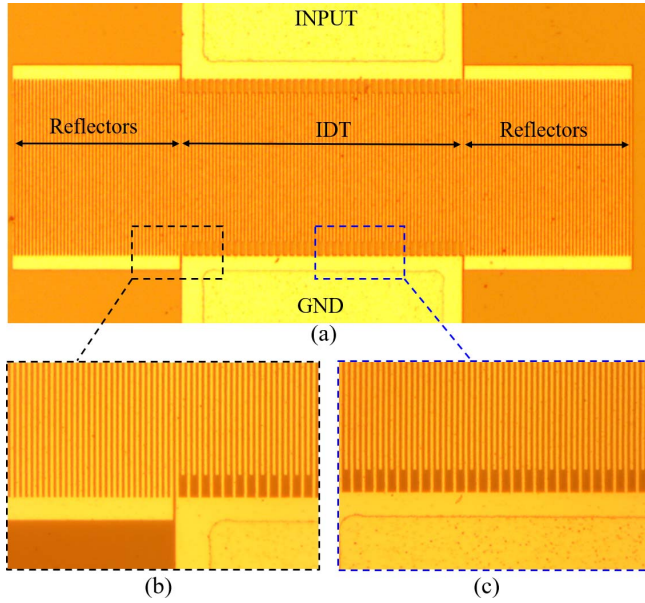


Fig. 7. Optical microscope images of the fabricated SH0 mode resonator. (a) Zoomed-out image of the resonator. (b) and (c) Zoomed-in images of different areas of the resonator.

evaporation, and lift-off process. Then photolithography was performed to open windows in busbar and pad areas for the evaporation of the second layer of aluminum, followed by the evaporation of the aluminum and the lift-off process. A Cooke E-Beam Evaporator was used for the aluminum evaporation, and the thickness of the first layer and the second layer of the evaporated aluminum are 130 and 275 nm, respectively. The optical images of the fabricated resonator (filter) are shown in Fig. 7 (8). The devices show good uniformity, and the IDTs and the reflectors are well defined with high fidelity.

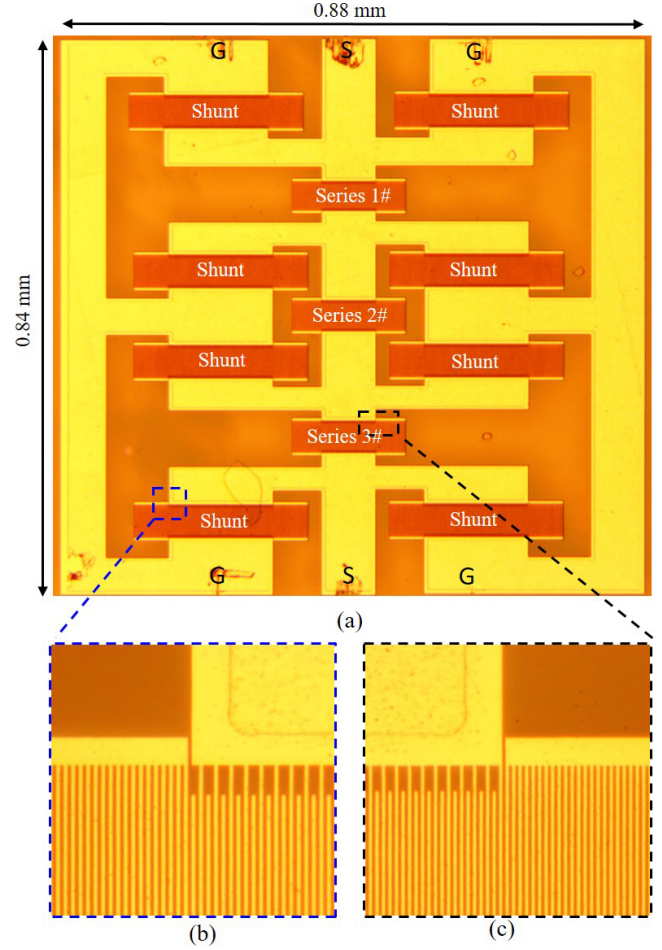
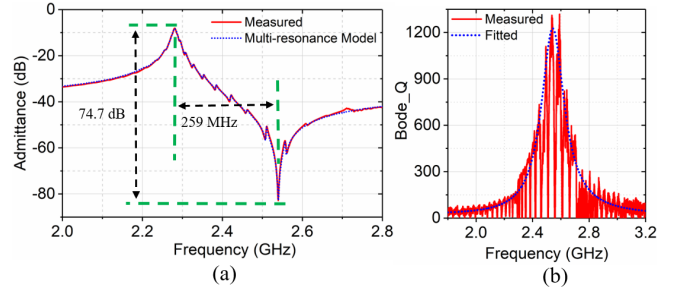


Fig. 8. Optical microscope images of the fabricated high-order ladder filter. (a) Zoomed-out image of the filter. (b) and (c) Zoomed-in images of different areas of the filter.



Symbol	f_s	k^2	C_0	Q_s	FoM
Value	2280 MHz	0.269	815 fF	154	330

Fig. 9. Measured and fitted (a) admittance responses and (b) Bode- Q of the fabricated SH0 mode resonator shown in Fig. 7. Some of the fitted parameters in the multiresonance model are listed in the inset table.

IV. MEASUREMENTS AND DISCUSSION

A. SH0 Mode Resonators

The fabricated devices were characterized at room temperature with a Keysight N5249A PNA network analyzer. The measured and fitted admittance responses and the quality factors (Bode- Q) of the resonator are shown in Fig. 9(a) and (b), respectively. As shown in Fig. 9(a), the resonator displays

TABLE IV
COMPARISON OF SOLIDLY MOUNTED ACOUSTIC RESONATORS

Ref	Substrate	k^2 (%)	Q_{max}	f_r (GHz)	FoM	ML
[3]	LiTaO ₃	8.0	1050	1.9	84	N
[45]	LiNbO ₃	7.0	1070	1.0	75	N
[4]	LiNbO ₃ on Si	7.5	1700	1.6	128	N
[3]	LiTaO ₃ on ML	9.8	4200	1.9	411	Y
[44]	LiNbO ₃ on ML	24.7	665	3.5	164	Y
This work	LiNbO₃ on SiC	26.9	1228	2.2	330	N

an SH0 mode resonance at 2.28 GHz with an extracted k^2 of 26.9%. The extracted static capacitance C_0 and the quality factor at resonant frequency Q_s (based on the multiresonance model [46]) are listed in the inset table of Fig. 9. It also shows an impedance ratio of 74.7 dB, defined by the impedance at the antiresonance f_a relative to that at the resonance f_r and an FBW of 10.4%, defined by the relative separation between f_r and f_a . Several transverse modes are also seen in the intended resonance, which may be mitigated by tilted resonators [47] or dummy electrodes [48]. The extracted f_r is slightly lower than the simulated result and the extracted k^2 is smaller than the simulated one. The following factors may cause this phenomenon: 1) the actual orientation of the device may deviate from the setting; 2) electrical loss of the electrodes; and 3) excited transverse modes. Fig. 9(b) shows a comparison of the measured and fitted Bode- Q and the agreement is good from 1.9 to 3.2 GHz. However, deteriorations are also seen in measured Bode- Q near f_a , which is caused by transverse modes. From the fitting results, the maximum Bode- Q near f_a is estimated as 1228, hence resulting in a high figure of merit (FoM) of 330 at 2.28 GHz.

A comparison between the above resonator and other mounted acoustic resonators [3], [4], [49], [50] is shown in Table IV. Although more optimizations are still required for transverse mode suppression and electrical loss, the device in this work has already demonstrated a quite high k^2 and Bode- Q . We believe that after reducing the electrical loss of the electrodes, the Bode- Q of our device will further increase. In [3] and [44], single-crystal piezoelectric films are bonded to multilayered (ML) substrates, which work as reflectors and confine the energy to the surfaces of those substrates, thus resulting in high Q . However, fabrication of the ML substrates is complicated and costly, and conductive layers (e.g., Pt) in the ML substrates typically require patterning to prevent unwanted capacitive coupling between the electrodes on the top surface.

Fig. 10(a) shows the measured admittance responses of the fabricated SH0 mode resonators with an IDT periodicity (λ) from 1.2 to 3.2 μm . In devices with $\lambda = 1.2$ and 1.4 μm , the Rayleigh wave is obvious, and its resonance is close to that of the intended SH0 wave. Increasing λ , that is, decreasing h/λ , can mitigate the effect of Rayleigh waves, as suggested in Fig. 2(b). Fig. 10(b) shows the resonances of the fabricated

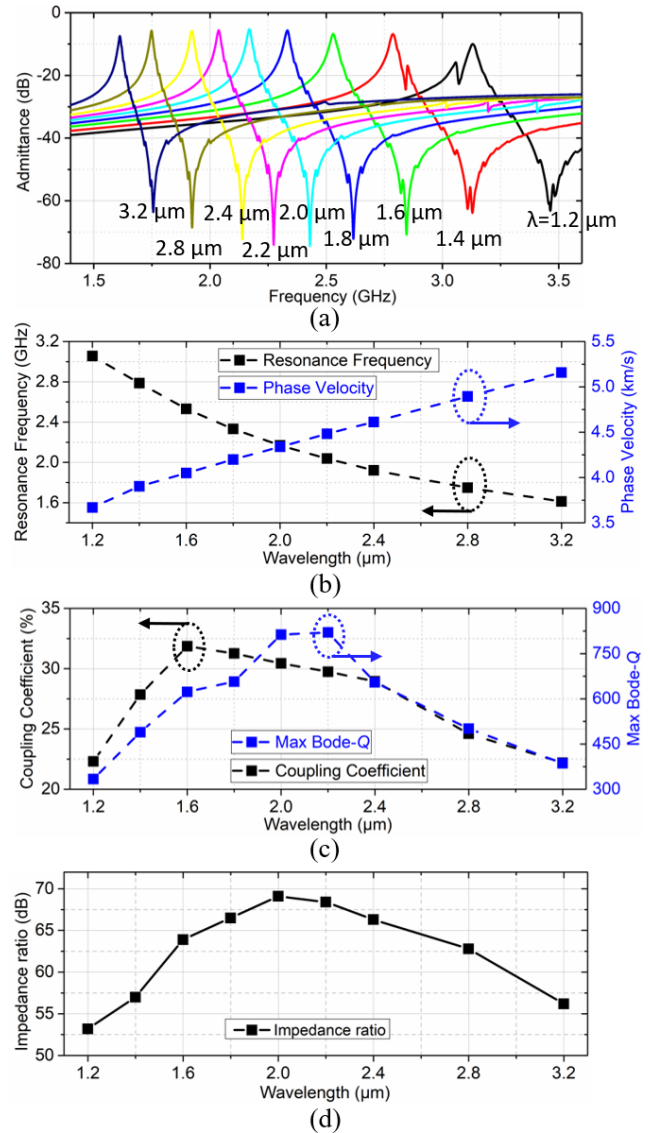


Fig. 10. Measured (a) admittance responses, (b) resonance frequencies and phase velocities, (c) electromechanical coupling (k^2) coefficients and quality factors (Bode- Q), and (d) impedance ratios of the fabricated SH0 resonators with different wavelengths.

resonators with different λ , ranging from 1.61 to 3.05 GHz, as well as the phase velocities, ranging from 3667 to 5158 m/s.

Fig. 10(c) shows the fitted electromechanical coupling (k^2) coefficients and the maximum Bode- Q of the fabricated resonators with different λ . The variation of the k^2 is caused by the wave (SH0) dispersion in a thin plate of LiNbO₃ and the energy penetration to the SiC substrate when λ is relatively large. As λ increases, the maximum Bode- Q increases first and then decreases. The increase in the maximum Bode- Q may be related to electrical loss. Note that these resonators were fabricated by a lift-off process, and smaller λ corresponds to narrower finger width. Therefore, the evaporated electrodes of narrower width may have larger resistivity, thus causing more significant electrical loss. Besides, the surface roughness may cause more severe scattering of the SH0 waves when λ is relatively small. As for the decrease in the maximum Bode- Q

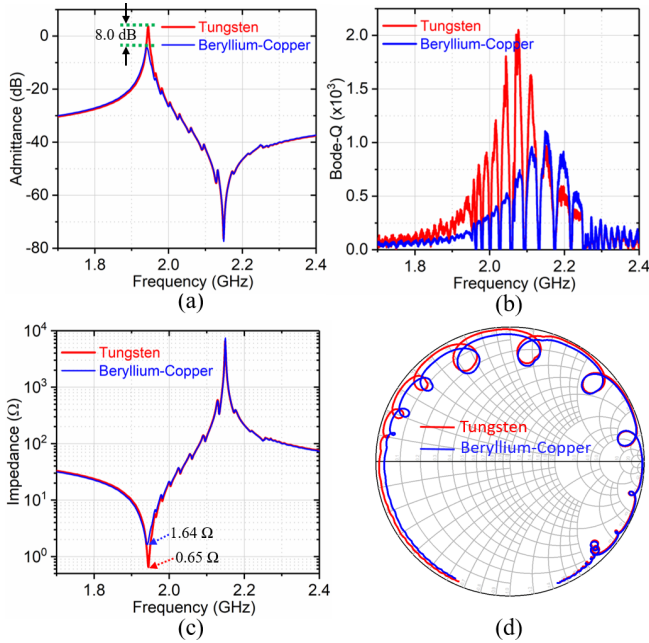


Fig. 11. Comparison of the measurement results of a fabricated SH0 mode resonator based on two types of RF probes. (a) Admittance. (b) Bode- Q . (c) Impedance. (d) Impedance on the Smith chart.

may be caused by the energy leakage to the SiC substrate when λ is relatively large.

Fig. 10(d) shows the measured impedance ratios of the fabricated resonators with different λ , from which we can find that as λ increases, the impedance ratio increases first and then decreases, which has the same trend as the maximum Bode- Q . The factors causing the variation of the maximum Bode- Q may also cause the variation of the impedance ratio.

B. Discussion on RF Measurements

The aluminum electrodes used in this work typically bear a thin layer of aluminum oxide, which introduces contact resistance in probe-based measurements. Unless a strain-gauge embedded probe is adopted, the contact resistance varies from one probe landing to another, thus resulting in uncertainties in the calibration and making accurate RF measurements of small impedance very difficult.

We used two types of RF probe: the first with tips made of beryllium-copper (BeCu) and the second with tips made of tungsten (W). Note that all the measurement results shown thus far are attained with the BeCu probes, which provide more stable and repeatable results. On the other hand, the stiffness of tungsten is three times greater than that of BeCu. Therefore, the tungsten probes can break the aluminum oxide layers more easily. In our experience, with proper contact pressure applied, the tungsten probe can punch through the aluminum oxide layers more thoroughly and form a better electrical contact with the aluminum electrodes, thus reducing the Q loading effect from the poor contact and impedance observed.

Fig. 11 shows the measurement results with the two types of probes. The admittance at the resonant frequency increase from -4.79 to 3.26 dB [Fig. 11(a)], while the corresponding

TABLE V
EXTRACTED PARAMETERS OF SHUNT AND SERIES RESONATORS

Param.	f_s (GHz)	k^2 (%)	L_m (nH)	R_m (Ω)	C_m (fF)	C_0 (fF)	R_s (Ω)	R_0 (Ω)
Shunt	2.05	27.6	19.3	0.293	312	1395	1.6	0
Series	2.28	26.9	27.4	0.357	178	815	2.0	0

impedance is reduced from 1.64 to 0.65 Ω [Fig. 11(c)] when switching from BeCu to W. The measured impedances on the Smith chart in Fig. 11(d) also show the same effect. It indicates that the Q of the presented resonator can be potentially even higher than so-far claimed values. As evidenced in Fig. 11(b), the measured Q is 2000, almost twice as the value attained with BeCu. However, we do not claim such value as probing with W tips has poor repeatability in our cases and the SLOT calibration may be less accurate. The lack of reproducibility arises from the fact that W probes can easily pick up aluminum and aluminum oxide from the probe pad, and have aluminum oxide build up on the tips. As a result, the contact resistance will gradually increase [51], and the mechanical damage of the electrode pads will be unavoidable and severe. In addition, the contact pressure is much more critical with tungsten probes than with BeCu probes [51], suggesting W probes needing more precise control to produce reliable results. Based on the above analysis, the remaining measurements are still done using the BeCu probes, which provide us with stable and repeatable results.

C. High-Order Ladder-Type Filter

The measured S-parameters of the fabricated filter (shown in Fig. 8) and the admittance responses of the build-in series and shunt resonators are shown in Fig. 12, and the extracted parameters of the shunt and the series (3#) resonators based on the MBVD model are listed in Table V. The measurements were performed with a 50 - Ω system impedance. As shown in Fig. 12(a), although the measured resonant frequency of the series resonators is slightly higher than the simulated value, the resonant frequency offset is well achieved. Besides, comparing the admittance curves of the three series resonators, we can find that the transverse modes of the same order are staggered from each other because of the variation of the aperture (shown in Table III). The measured S_{21} and S_{11} of the filter are shown in Fig. 12(b), which shows an IL of 1.38 dB, a 3-dB FBW of 9.9%, and an out-of-band rejection of 41.6 dB at 1 GHz from the center frequency. The measured return loss at the center frequency is about 10 dB, which is seriously decreased by the in-band ripples (transverse modes). Note that the upper band transmission zero has disappeared in the measurement response shown in Fig. 12(b), which may arise from the fact that some energy is coupled from the source to the load or from imperfect grounding [52]–[54]. The measured group delay response of the filter is shown in Fig. 12(c). The in-band group delay is less than 12 ns but with substantial variations that cause distortions to RF signals. The group delay ripples are induced by the transverse spurious

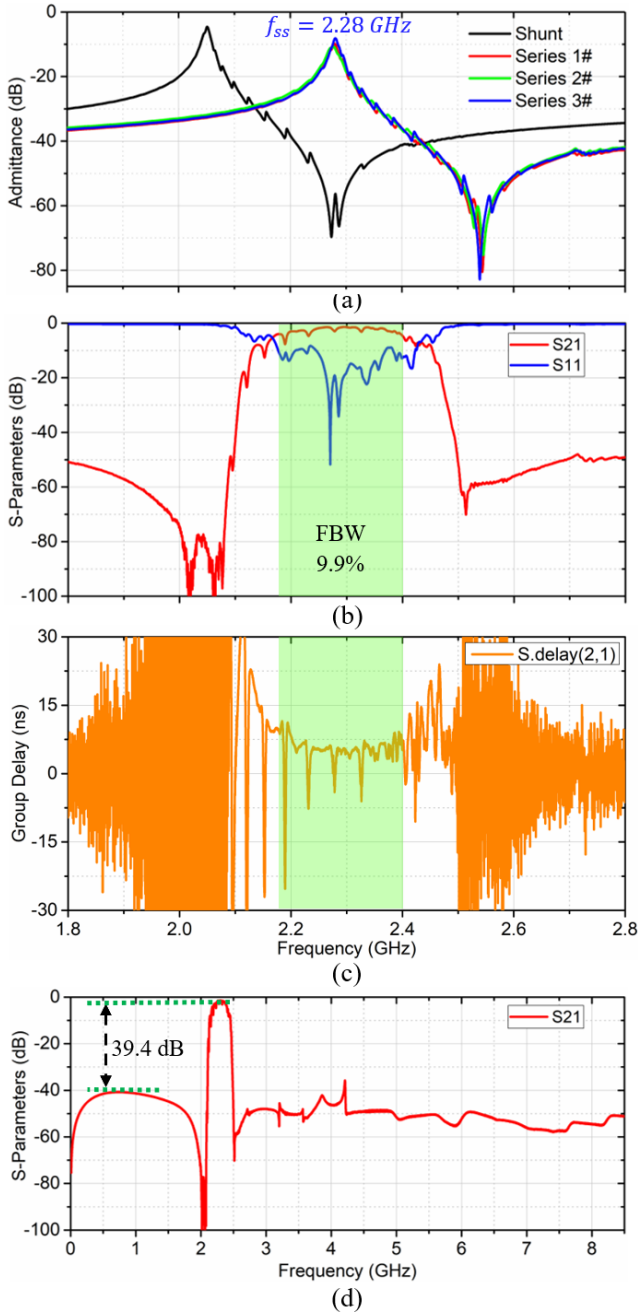


Fig. 12. (a) Measured admittance responses of the series and shunt resonators. (b) Measured S-parameters (S_{11} and S_{21}) of the fabricated filter. (c) Measured group delay of the fabricated filter. (d) Measured S-parameter (S_{21}) of the fabricated filter over a wide frequency range.

modes of the series and shunt resonators. Several methods have been reported to mitigate or suppress the transverse modes, such as apodized IDT electrodes [41], dummy electrodes [48], and the tilted transducers [55], which will be studied in our future work. Besides, the fabricated filter shows a spurious-free response over a wide frequency range from 10 MHz to 8.5 GHz, as shown in Fig. 12(d). Comparing the magnitude of the in-band IL ripples on the left and right parts, we can find that shifting the same order transverse modes of the build-in resonators can help to mitigate the in-band ripples. Although the magnitude of the in-band IL ripples is relatively large due

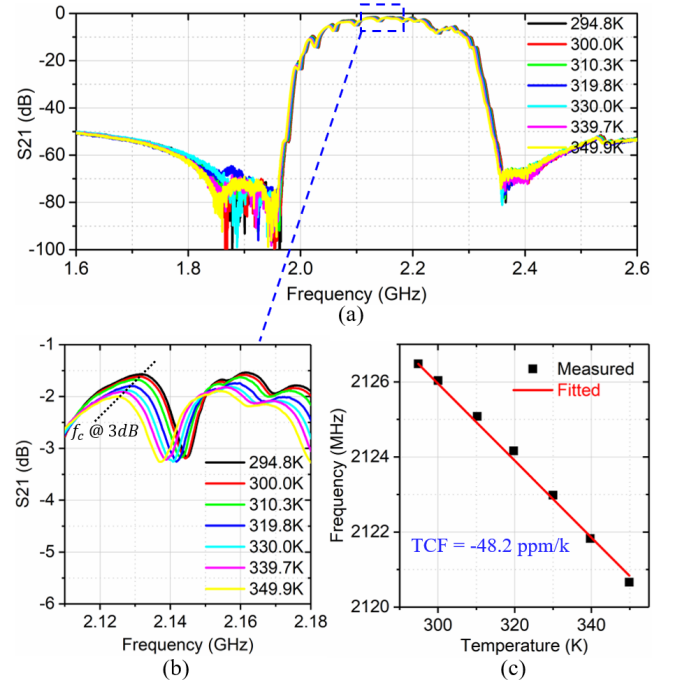


Fig. 13. Temperature characteristics of a fabricated filter. (a) IL. (b) Zoomed-in IL. (c) Center frequency variation and the extracted TCF in the temperature range of 295–350 K.

TABLE VI
COMPARISON OF SOLIDLY MOUNTED ACOUSTIC FILTERS

Ref	Substrate	f_c (GHz)	FBW (%)	IL (dB)	OoB (dB)	TCF (ppm/k)
[49]	LiNbO ₃	2.49	6.2	3.5	20.0	/
[50]	LiNbO ₃ on Diamond-Silicon*	2.32	1.0	28.0	20.0	/
[3]	LiTaO ₃ on ML	1.88	4.8	0.8	35.0	-8.0
[51]	LiTaO ₃ on ML	2.44	4.1	0.9	45.0	/
This work	LiNbO₃ on SiC	2.29	9.9	1.38	41.6	-48.2

* Sputtered LiNbO₃ thin films on the diamond-coated silicon, in which the diamond films are also sputtered.

to the strong transverse modes, the above filter still shows good performance.

D. Temperature Characteristics

The filter with the topology shown in Fig. 5(c) and a center frequency of 2.12 GHz were measured at different temperatures, ranging from 295 to 350 K. The measured S_{21} and the extracted TCF are shown in Fig. 13. As shown in Fig. 13(a) and (b), the passband drifts to lower frequencies due to the negative temperature coefficient of stiffness of the LiNbO₃ thin film [56] and the SiC substrate [57]. The temperature coefficient of the center frequency (TCF) is plotted in Fig. 13(c), showing a fitted TCF around -48.2 ppm/K. The result shows good linearity over the measured frequency range.

A comparison between the fabricated filter (with a center frequency of 2.29 GHz) and other solidly mounted acoustic filters [3], [58], [59], [60] is shown in Table VI. Although

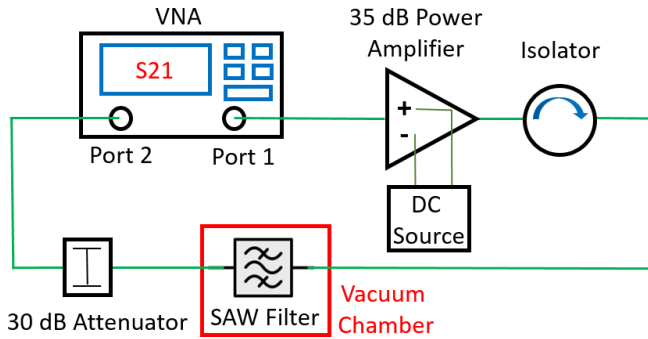
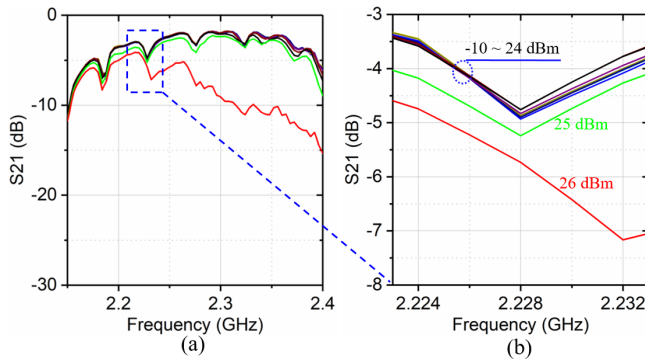


Fig. 14. Setup for power handling measurement.

Fig. 15. Measured power handling performance of the fabricated filter. (a) S_{21} . (b) Zoomed-in S_{21} .

more optimizations are still required for transverse mode suppression and TCF, the filter in this work has already demonstrated a quite large FBW and a decent IL with respect to an OoB rejection of 41.6 dB. In [3] and [51], single-crystal LiTaO₃ films are bonded to ML substrates, in which an intermediate layer of SiO₂ is applied for temperature compensation. Due to the smaller TCF of LiTaO₃ than LiNbO₃ and the temperature compensation layer, the filter (shown in [3]) built on the LiTaO₃-on-ML substrate exhibits a good TCF. However, LiTaO₃ itself has weaker electromechanical coupling than LiNbO₃, which will limit the bandwidth of LiTaO₃-based devices, thus limiting its application in the growing wideband applications. In [50], LiNbO₃ films are sputtered on the diamond-coated silicon substrates. Due to the limited crystalline quality of the sputtered LiNbO₃ films and the diamond films, the built filter shows poor performance, which highlights ion-slicing and wafer-bonding processes.

E. Power Handling

The schematic of the power handling measurement circuit is shown in Fig. 14. The measured power handling performance of the filter is shown in Fig. 15. As shown in Fig. 15(b), when the power applied to the filter increases from -10 to 24 dBm, the variation of S_{21} is less than 0.2 dB, which suggests good thermal stability and sufficient heat dissipation through LiNbO₃ on SiC substrates. When the applied power increases to 25 dBm, the performance degradation becomes more pronounced, and the S_{21} decreases by an additional 0.3 dB. Furthermore, when the applied power increases to

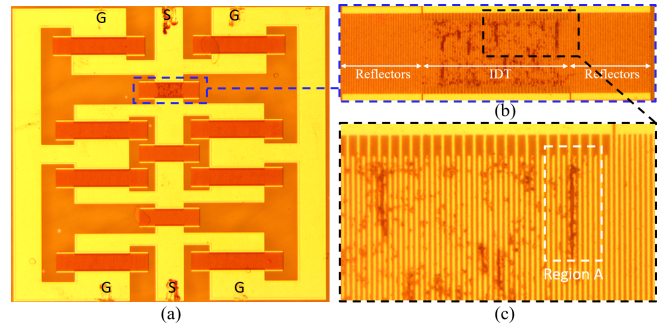


Fig. 16. Optical images of the filter after the power handling measurement.

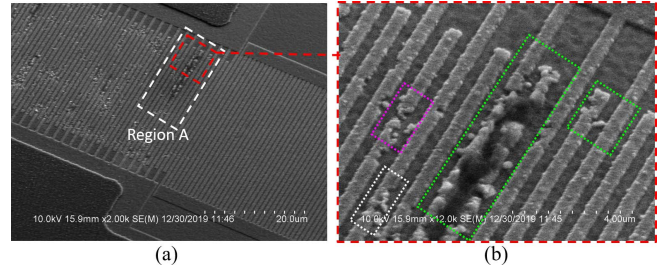


Fig. 17. SEM images of the filter after the power handling measurement.

26 dBm, the filter shows significant irreversible performance degradation and eventually fails. The failure starts near the resonant frequency (f_{ss} , 2.28 GHz) of the series resonators. This is anticipated as the series resonators withstand more power relative to the shunt ones, and are therefore more prone to breakdown.

After the power handling measurements, the measured filter was examined under an optical microscope and a scanning electron microscope (SEM). The optical images and the SEM images are shown in Figs. 16 and 17, respectively. As shown in Fig. 16(a), the first series resonator exhibits damages in some areas of the active region. The zoomed-in images in Fig. 16(b) and (c) clearly indicate that the interdigital aluminum electrodes have been degraded, including material spreading of the electrodes and shorting between two adjacent electrodes. Fig. 17(a) shows the corresponding SEM image of the resonator shown in Fig. 16(b), while the zoomed-in SEM image shown in Fig. 17(b) depicts Region A in Figs. 16(b) and 17(a). As marked in Fig. 17(b), three types of damages are observed: 1) aluminum spreading without breaking the electrical continuity of an electrode (e.g., the electrode marked by the white-dashed rectangular); 2) aluminum melting or rupture breaking the electrical continuity of an electrode (e.g., area marked by the purple-dashed box); and 3) shorting between two adjacent electrodes of opposite polarity (e.g., the electrodes marked by the green dashed box).

The transducer electrodes of high-frequency SAW devices can be damaged by dc voltage pulses and metal melting, rupture or splattering may be observed due to arc discharge (metal to metal discharge) [61], [62]. Besides, temperature rise and continuous heavy cyclic stress at the interface between IDTs and substrates will result in Al atoms migrating and thus forming rupture (extrusions and voids) of the electrodes,

which is called acoustomigration [63]. The metal melting and rupture that do not cause an electrical short [e.g., area in the white-dashed or pink-dashed box] represents a surface irregularity for the traveling acoustic waves. The degradation of the filter performance (S_{21}) is inevitable if such discontinuities occur. When the melted and splattered metal globules or the ruptured metal happen to be in the interelectrode regions in the active region (e.g., the electrodes marked by the green dashed box), the shorting between adjacent electrodes may occur, which will significantly degrade the filter performance and may cause the failure of the filter. In our measurements, when the applied power increases to 25 dBm, the performance degradation becomes obvious, and the corresponding S_{21} decreases by 0.3 dB, which may be caused by the melted or ruptured but not shorted electrodes. When the applied power increases to 26 dBm, the filter shows the significant performance degradation and gradually fails, which may be caused by the shorted electrodes.

In this work, several reasons may cause the damage of the aluminum electrodes, which degrade the power handling performance of the filter. First, the Al atoms migration (acoustomigration) may form extrusions and voids in IDTs. Second, the transferred LiNbO₃ thin films for device fabrication are unreduced, as well as the single-crystal LiNbO₃ wafer used for wafer bonding. So there may be a strong electrostatic field at the surface of the transferred LiNbO₃ thin films when the temperature changes due to pyroelectric charging effects [64], [65], which may stimulate or enhance the arc discharge. Besides, the electrode material, aluminum, which naturally forms an oxide surface layer, would be especially susceptible to high rates of electron emission [66], which may stimulate or enhance the arc discharge, too. Based on the above analysis, to mitigate the electrode damage caused by the arc discharge and to improve the power handling performance, it is better to use the reduced LiNbO₃ wafers for bonding. The reduction process increases the dc electrical conductivity of the wafer, thus mitigating the spurious pyroelectric charging effects during thermal cycling [64]. Meanwhile, strengthened electrodes will suppress acoustomigration in IDTs and thus improving the power durability of acoustic filters, such as Al alloy [67], [68], layered structure [67], [69], highly textured Al film [70]–[72], and passivation layer [73], [74]. We believe that power handling is limited predominately by the electrodes, and has not yet reached the thermal nonlinearity limit. With improved processing and strengthened electrodes, power handling might be further enhanced to expose the benefits of having SiC as substrates.

V. CONCLUSION

In this work, we have demonstrated a group of SH0 mode surface acoustic wave resonators and a group of filters based on the SH0 mode resonators using LiNbO₃ thin films on SiC substrates. The single-crystalline X-cut LiNbO₃ thin films onto the 4H-SiC substrates have been prepared by ion-slicing and wafer-bonding processes. Thanks to the excellent piezoelectric properties of the LiNbO₃ thin film and the desirable mix of mechanical properties of the SiC substrate. The fabricated

resonator has demonstrated a k^2 of 26.9%, a quality factor of 1228, and an FoM of 330 at 2.28 GHz. Additionally, resonators with resonances from 1.61 to 3.05 GHz have been studied, which show the impedance ratios between 53.2 and 74.7 dB. Filters based on the SH0 resonators have been demonstrated at 2.29 GHz with an excellent FBW, a good OoB rejection, a low IL, and a spurious-free response over a wide frequency range. Besides, the fabricated filters also show a TCF of -48.2 ppm/°C and a power handling of 25 dBm. Although the composition and the process of the interdigital electrodes need to be optimized to obtain greater power handling, and the geometry of the IDT fingers should also be optimized to mitigate or suppress the transverse spurious modes, the demonstrations still show that acoustic devices on the LiNbO₃ on SiC platform have great potential for radio-frequency applications.

ACKNOWLEDGMENT

The authors would like to thank Edmond Chow in Micro and Nano-Technology Laboratory, College of Engineer, University of Illinois at Urbana Champaign, Urbana, IL, USA, for performing the e-beam lithography in this work.

REFERENCES

- [1] M. Levy *et al.*, "Fabrication of single-crystal lithium niobate films by crystal ion slicing," *Appl. Phys. Lett.*, vol. 73, no. 16, pp. 2293–2295, Oct. 1998.
- [2] S. Gong and G. Piazza, "Design and analysis of Lithium-Niobate-based high electromechanical coupling RF-MEMS resonators for wideband filtering," *IEEE Trans. Microw. Theory Techn.*, vol. 61, no. 1, pp. 403–414, Jan. 2013.
- [3] T. Takai *et al.*, "High-performance SAW resonator on new multilayered substrate using LiTaO₃ crystal," *IEEE Trans. Ultrason., Ferroelectr., Freq. Control*, vol. 64, no. 9, pp. 1382–1389, Sep. 2017.
- [4] T. Pastureauud *et al.*, "High-frequency surface acoustic waves excited on thin-oriented LiNbO₃ single-crystal layers transferred onto silicon," *IEEE Trans. Ultrason., Ferroelectr., Freq. Control*, vol. 54, no. 4, pp. 870–876, Apr. 2007.
- [5] Y.-H. Song and S. Gong, "Elimination of spurious modes in SH0 lithium niobate laterally vibrating resonators," *IEEE Electron Device Lett.*, vol. 36, no. 11, pp. 1198–1201, Nov. 2015.
- [6] M.-H. Li, R. Lu, T. Manzanque, and S. Gong, "Low phase noise RF oscillators based on thin-film lithium niobate acoustic delay lines," *J. Microelectromech. Syst.*, vol. 29, no. 2, pp. 129–131, Apr. 2020.
- [7] T. Kimura *et al.*, "A high velocity and wideband SAW on a thin LiNbO₃ plate bonded on a Si substrate in the SHF range," in *Proc. IEEE Int. Ultrason. Symp. (IUS)*, Oct. 2019, pp. 1239–1248.
- [8] R. Lu, Y. Yang, M. Li, and S. Gong, "GHz low-loss acoustic RF couplers in lithium Niobate thin film," *IEEE Trans. Ultrason., Ferroelectr., Freq. Control*, early access, Feb. 3, 2020, doi: [10.1109/TUFFC.2020.2971196](https://doi.org/10.1109/TUFFC.2020.2971196).
- [9] Y. Yang, R. Lu, and S. Gong, "A 1.65 GHz lithium Niobate A1 resonator with electromechanical coupling of 14% and Q of 3112," in *Proc. IEEE 32nd Int. Conf. Micro Electro Mech. Syst. (MEMS)*, Jan. 2019, pp. 875–878.
- [10] Y. Yang, R. Lu, and S. Gong, "High Q antisymmetric mode lithium Niobate MEMS resonators with spurious mitigation," *J. Microelectromech. Syst.*, vol. 29, no. 2, pp. 135–143, Apr. 2020.
- [11] M. Kadota and S. Tanaka, "Wideband acoustic wave resonators composed of hetero acoustic layer structure," *Jpn. J. Appl. Phys.*, vol. 57, no. 7S1, Jul. 2018, Art. no. 07LD12, doi: [10.7567/JJAP.57.07LD12](https://doi.org/10.7567/JJAP.57.07LD12).
- [12] N. Naumenko, "LiNbO₃ plate bonded to quartz as a substrate for high frequency wideband SAW devices," in *Proc. IEEE Int. Ultrason. Symp. (IUS)*, Oct. 2019, pp. 1227–1230.
- [13] H. J. McSkimin and P. Andreatch, "Elastic Moduli of diamond as a function of pressure and temperature," *J. Appl. Phys.*, vol. 43, no. 7, pp. 2944–2948, Jul. 1972.
- [14] E. A. Burgemeister, "Thermal conductivity of natural diamond between 320 and 450 k," *Phys. B+C*, vol. 93, no. 2, pp. 165–179, Feb. 1978.

- [15] K. Kamitani, M. Grimsditch, J. C. Nipko, C.-K. Loong, M. Okada, and I. Kimura, "The elastic constants of silicon carbide: A Brillouin-scattering study of 4H and 6H SiC single crystals," *J. Appl. Phys.*, vol. 82, no. 6, pp. 3152–3154, Sep. 1997.
- [16] V. Bougrov, M. Levinshtein, S. L. Rumyantsev, and A. Zubrilov, *Properties of Advanced Semiconductor Materials GaN, AlN, InN, BN, SiC, SiGe*, M. E. Levinshtein, S. L. Rumyantsev, and M. S. Shur, Eds. New York, NY, USA: Wiley, 2001, pp. 1–30.
- [17] D. T. Bell and R. C. M. Li, "Surface-acoustic-wave resonators," *Proc. IEEE*, vol. 64, no. 5, pp. 711–721, May 1976.
- [18] G. Kovacs, M. Anhorn, H. E. Engan, G. Visintini, and C. C. W. Ruppel, "Improved material constants for LiNbO₃ and LiTaO₃," in *Proc. IEEE Int. Ultrason. Symp.*, Dec. 1990, pp. 435–438.
- [19] K. K. Wong, *Properties of Lithium Niobate*. London, U.K.: The Institution of Electrical Engineers, 2002.
- [20] Y. S. Kim and R. T. Smith, "Thermal expansion of lithium tantalate and lithium Niobate single crystals," *J. Appl. Phys.*, vol. 40, no. 11, pp. 4637–4641, Oct. 1969.
- [21] S. Nikanorov, Y. A. Burenkov, and A. Stepanov, "Elastic properties of Si," *Sov. Phys. Solid State*, vol. 13, no. 10, pp. 2516–2518, 1972.
- [22] C. J. Glassbrenner and G. A. Slack, "Thermal conductivity of silicon and germanium from 3 K to the melting point," *Phys. Rev.*, vol. 134, no. 5, pp. 1743–1748, Jun. 1964.
- [23] Y. Okada and Y. Tokumaru, "Precise determination of lattice parameter and thermal expansion coefficient of silicon between 300 and 1500 K," *J. Appl. Phys.*, vol. 56, no. 2, pp. 314–320, Jul. 1984.
- [24] K. A. Pestka, J. D. Maynard, D. Gao, and C. Carraro, "Measurement of the elastic constants of a columnar SiC thin film," *Phys. Rev. Lett.*, vol. 100, no. 5, Feb. 2008, doi: [10.1103/PhysRevLett.100.055503](https://doi.org/10.1103/PhysRevLett.100.055503).
- [25] I. Petousis *et al.*, "High-throughput screening of inorganic compounds for the discovery of novel dielectric and optical materials," *Sci. Data*, vol. 4, no. 1, pp. 1–12, Jan. 2017.
- [26] M. I. Lei and M. Mehregany, "Characterization of thermoelectric properties of heavily doped n-Type polycrystalline silicon carbide thin films," *IEEE Trans. Electron Devices*, vol. 60, no. 1, pp. 513–517, Jan. 2013.
- [27] S. Roy, R. G. DeAnna, C. A. Zorman, and M. Mehregany, "Fabrication and characterization of polycrystalline SiC resonators," *IEEE Trans. Electron Devices*, vol. 49, no. 12, pp. 2323–2332, Dec. 2002.
- [28] K. Tolpygo, "Optical, elastic and piezoelectric properties of ionic and valence crystals with the ZnS type lattice," *Sov. Phys. Solid State*, vol. 2, no. 10, pp. 2367–2376, 1961.
- [29] Z. Li and R. C. Bradt, "Thermal expansion and thermal expansion anisotropy of SiC polytypes," *J. Amer. Ceram. Soc.*, vol. 70, no. 7, pp. 445–448, Jul. 1987.
- [30] D. F. Gibbs and G. J. Hill, "The variation of the dielectric constant of diamond with pressure," *Phil. Mag.*, vol. 9, no. 99, pp. 367–375, Mar. 1964.
- [31] G. A. Slack and S. F. Bartram, "Thermal expansion of some diamondlike crystals," *J. Appl. Phys.*, vol. 46, no. 1, pp. 89–98, Jan. 1975.
- [32] B. T. Bernstein, "Elastic constants of synthetic sapphire at 27° C," *J. Appl. Phys.*, vol. 34, no. 1, pp. 169–172, Jan. 1963.
- [33] E. R. Dobrovinskaya, L. A. Lytvynov, and V. Pishchik, "Properties of sapphire," in *Sapphire*. Berlin, Germany: Springer, 2009, pp. 55–176.
- [34] R. Bechmann, "Elastic and piezoelectric constants of alpha-quartz," *Phys. Rev.*, vol. 110, no. 5, pp. 1060–1061, Jun. 1958.
- [35] K.-I. Horai and G. Simmons, "Thermal conductivity of rock-forming minerals," *Earth Planet. Sci. Lett.*, vol. 6, no. 5, pp. 359–368, Jan. 1969.
- [36] J. A. Kosinski, J. G. Gualtieri, and A. Ballato, "Thermal expansion of alpha quartz," in *Proc. 45th Annu. Symp. Freq. Control*, May 1991, pp. 22–28.
- [37] M. Tomar, V. Gupta, and K. Sreenivas, "Temperature coefficient of elastic constants of SiO₂ over-layer on LiNbO₃ for a temperature stable SAW device," *J. Phys. D, Appl. Phys.*, vol. 36, no. 15, pp. 1773–1777, Jul. 2003.
- [38] B. El-Kareh, *Fundamentals of Semiconductor Processing Technology*. Boston, MA, USA: Springer, 1995.
- [39] T. C. T. Ting, "Longitudinal and transverse waves in anisotropic elastic materials," *Acta Mechanica*, vol. 185, nos. 3–4, pp. 147–164, Sep. 2006.
- [40] T. C. T. Ting, "Transverse waves in anisotropic elastic materials," *Wave Motion*, vol. 44, no. 2, pp. 107–119, Dec. 2006.
- [41] T. Kimura, K. Daimon, T. Ogami, and M. Kadota, "S0Mode Lamb wave resonators using LiNbO₃ thin plate on acoustic multilayer reflector," *Jpn. J. Appl. Phys.*, vol. 52, no. 7S, Jul. 2013, Art. no. 07HD03.
- [42] I. E. Kuznetsova, B. D. Zaitsev, S. G. Joshi, and I. A. Borodina, "Investigation of acoustic waves in thin plates of lithium niobate and lithium tantalate," *IEEE Trans. Ultrason., Ferroelectr., Freq. Control*, vol. 48, no. 1, pp. 322–328, Jan. 2001.
- [43] K. Hashimoto, H. Kamizuma, M. Watanabe, T. Omori, and M. Yamaguchi, "Wavenumber domain analysis of two-dimensional SAW images captured by phase-sensitive laser probe system," *IEEE Trans. Ultrason., Ferroelectr., Freq. Control*, vol. 54, no. 5, pp. 1072–1075, May 2007.
- [44] K.-Y. Hashimoto, *RF Bulk Acoustic Wave Filters for Communications*. Norwood, MA, USA: Artech House, 2009.
- [45] Y. Shuai *et al.*, "Fabrication of Y128- and Y36-cut lithium niobate single-crystalline thin films by crystal-ion-slicing technique," *Jpn. J. Appl. Phys.*, vol. 57, no. 4S, Apr. 2018, Art. no. 04FK05, doi: [10.7567/JJAP.57.04FK05](https://doi.org/10.7567/JJAP.57.04FK05).
- [46] R. Lu, M.-H. Li, Y. Yang, T. Manzanique, and S. Gong, "Accurate extraction of large electromechanical coupling in piezoelectric MEMS resonators," *J. Microelectromech. Syst.*, vol. 28, no. 2, pp. 209–218, Apr. 2019.
- [47] H. Iwamoto, T. Takai, Y. Takamine, T. Nakao, T. Fuyutsume, and M. Koshino, "Transverse modes in I.H.P. SAW resonator and their suppression method," in *Proc. IEEE Int. Ultrason. Symp. (IUS)*, Oct. 2018, pp. 1–4, doi: [10.1109/ULTSYM.2018.8580175](https://doi.org/10.1109/ULTSYM.2018.8580175).
- [48] H. Zhang, J. Liang, X. Zhou, H. Zhang, D. Zhang, and W. Pang, "Transverse mode spurious resonance suppression in Lamb wave MEMS resonators: Theory, modeling, and experiment," *IEEE Trans. Electron Devices*, vol. 62, no. 9, pp. 3034–3041, Sep. 2015.
- [49] T. Kimura, Y. Kishimoto, M. Omura, and K.-Y. Hashimoto, "3.5 GHz longitudinal leaky surface acoustic wave resonator using a multilayered waveguide structure for high acoustic energy confinement," *Jpn. J. Appl. Phys.*, vol. 57, no. 7S1, Jul. 2018, Art. no. 07LD15, doi: [10.7567/JJAP.57.07LD15](https://doi.org/10.7567/JJAP.57.07LD15).
- [50] T. Nakao *et al.*, "Smaller surface acoustic wave duplexer for US personal communication service having good temperature characteristics," *Jpn. J. Appl. Phys.*, vol. 46, no. 7B, pp. 4760–4763, Jul. 2007.
- [51] J.-L. Carbonero, G. Morin, and B. Cabon, "Comparison between beryllium-copper and tungsten high frequency air coplanar probes," *IEEE Trans. Microw. Theory Techn.*, vol. 43, no. 12, pp. 2786–2793, Jan. 1995.
- [52] J. Tsutsumi *et al.*, "A design technique to enhance isolation of duplexer in single-ended and differential modes," in *Proc. IEEE Int. Ultrason. Symp.*, Oct. 2011, pp. 1833–1836, doi: [10.1109/ULTSYM.2011.0458](https://doi.org/10.1109/ULTSYM.2011.0458).
- [53] A. Gimenez and P. de Paco, "Involving source-load leakage effects to improve isolation in ladder acoustic wave filters," in *IEEE MTT-S Int. Microw. Symp. Dig.*, May 2016, pp. 1–4, doi: [10.1109/MWSYM.2016.7540149](https://doi.org/10.1109/MWSYM.2016.7540149).
- [54] A. Triano, J. Verdu, P. de Paco, T. Bauer, and K. Wagner, "Relation between electromagnetic coupling effects and network synthesis for AW ladder type filters," in *Proc. IEEE Int. Ultrason. Symp. (IUS)*, Sep. 2017, pp. 1–4, doi: [10.1109/ULTSYM.2017.8091644](https://doi.org/10.1109/ULTSYM.2017.8091644).
- [55] H. Iwamoto, T. Takai, Y. Takamine, T. Nakao, T. Fuyutsume, and M. Koshino, "Transverse modes in I.H.P. SAW resonator and their suppression method," in *Proc. IEEE Int. Ultrason. Symp. (IUS)*, Dec. 2018, pp. 1–4, doi: [10.1109/ULTSYM.2018.8580175](https://doi.org/10.1109/ULTSYM.2018.8580175).
- [56] R. T. Smith and F. S. Welsh, "Temperature dependence of the elastic, piezoelectric, and dielectric constants of lithium tantalate and lithium niobate," *J. Appl. Phys.*, vol. 42, no. 6, pp. 2219–2230, May 1971.
- [57] Z. Li and R. C. Bradt, "The single crystal elastic constants of hexagonal SiC to 1000° C," *Int. J. High Technol. Ceram.*, vol. 4, no. 1, pp. 1–10, Jan. 1988.
- [58] T. Makkonen, V. P. Plessky, W. Steichen, and M. M. Salomaa, "Surface-acoustic-wave devices for the 2.5-5 GHz frequency range based on longitudinal leaky waves," *Appl. Phys. Lett.*, vol. 82, no. 19, pp. 3351–3353, May 2003.
- [59] E. Dogheche, D. Remiens, S. Shikata, A. Hachigo, and H. Nakahata, "High-frequency surface acoustic wave devices based on LiNbO₃/diamond multilayered structure," *Appl. Phys. Lett.*, vol. 87, no. 21, Nov. 2005, Art. no. 213503, doi: [10.1063/1.2135383](https://doi.org/10.1063/1.2135383).
- [60] T. Takai *et al.*, "High-performance SAW resonator with simplified LiTaO₃/SiO₂ double layer structure on Si substrate," *IEEE Trans. Ultrason., Ferroelectr., Freq. Control*, vol. 66, no. 5, pp. 1006–1013, May 2019.
- [61] F. S. Hickernell, "DC voltage effects on SAW device interdigital electrodes," in *Proc. 15th Int. Rel. Phys. Symp.*, Apr. 1977, pp. 144–148.
- [62] F. S. Hickernell, P. L. Clar, and I. R. Cook, "Pulsed DC voltage breakdown between interdigital electrodes," in *Proc. Ultrason. Symp.*, 1972, pp. 388–391.

- [63] T. Hesjedal, J. Mohanty, F. Kubat, W. Ruile, and L. M. Reindl, "A microscopic view on acoustomigration," *IEEE Trans. Ultrason., Ferroelectr., Freq. Control*, vol. 52, no. 9, pp. 1584–1593, Sep. 2005.
- [64] P. F. Bordui, D. H. Jundt, E. M. Standifer, R. G. Norwood, R. L. Sawin, and J. D. Galipeau, "Chemically reduced lithium niobate single crystals: Processing, properties and improved surface acoustic wave device fabrication and performance," *J. Appl. Phys.*, vol. 85, no. 7, pp. 3766–3769, Apr. 1999.
- [65] B. Rosenblum, P. Bräunlich, and J. P. Carrico, "Thermally stimulated field emission from pyroelectric LiNbO₃," *Appl. Phys. Lett.*, vol. 25, no. 1, pp. 17–19, Jul. 1974.
- [66] F. S. Hickernell and J. J. Crawford, "Voltage breakdown characteristics of close spaced aluminum arc gap structures on oxidized silicon," in *Proc. 15th Int. Rel. Phys. Symp.*, Apr. 1977, pp. 128–131.
- [67] R. Takayama, H. Nakanishi, and K. Hashimoto, "Impact of composition and structure of Al alloy electrodes to power durability of SAW devices," in *Proc. IEEE Int. Ultrason. Symp.*, Sep. 2014, pp. 886–892.
- [68] R. Nüssl *et al.*, "Enhanced stress durability of nano resonators with scandium doped electrodes," *Mater. Characterization*, vol. 61, no. 11, pp. 1054–1060, Nov. 2010.
- [69] T. Nishihara, H. Uchishiba, T. Matsuda, O. Ikata, and Y. Satoh, "Improvement in power durability of SAW filters," in *Proc. IEEE Ultrason. Symp. Int. Symp.*, Nov. 1995, pp. 383–388.
- [70] R. Nüssl, T. Jewula, W. Ruile, T. Sulima, and W. Hansch, "Correlation between texture and mechanical stress durability of thin aluminum films," *Thin Solid Films*, vol. 556, pp. 376–380, Apr. 2014.
- [71] A. Kamijo and N. Matsukura, "High resistance to stress-migration of [111] textured Al electrodes for surface acoustic wave devices," *AIP Conf. Proc.*, vol. 418, no. 1, pp. 239–249, 1998.
- [72] S. Fu *et al.*, "Texture-enhanced Al-cu electrodes on ultrathin Ti buffer layers for high-power durable 2.6 GHz SAW filters," *AIP Adv.*, vol. 8, no. 4, Apr. 2018, Art. no. 045212, doi: [10.1063/1.5017091](https://doi.org/10.1063/1.5017091).
- [73] B. W. Marks, D. W. Sheddric, and S. Jen, "Impact of SAW device passivation on RF performance," *IEEE Trans. Ultrason., Ferroelectr., Freq. Control*, vol. 48, no. 5, pp. 1362–1366, Sep. 2001.
- [74] J. Y. Kim, H. J. Kim, H. M. Cho, H. K. Yang, and J. C. Park, "Passivation layer effects on power durability of SAW duplexer," in *Proc. IEEE Ultrason. Symp. Int. Symp.*, Oct. 1999, pp. 39–42.



Shibin Zhang (Member, IEEE) received the B.E. degree in electronic science and technology from Southeast University, Nanjing, China, in 2015. He is currently pursuing the Ph.D. degree in microelectronics and solid state electronics at the Shanghai Institute of Microsystem and Information Technology, Chinese Academy of Sciences, Beijing, China.

He was a Visiting Scholar with the Micro and Nanotechnology Laboratory, University of Illinois at Urbana–Champaign, Urbana, IL, USA. His current research interests include the design and microfabrication techniques of MEMS resonators and filters for RF front ends.



Ruochen Lu (Member, IEEE) received the B.E. degree (Hons.) in microelectronics from Tsinghua University, Beijing, China, in 2014, and M.S. and Ph.D. degrees in electrical engineering from the University of Illinois at Urbana–Champaign, Urbana, IL, USA, in 2017 and 2019, respectively.

He is currently a Post-Doctoral Researcher with University of Illinois at Urbana–Champaign. His research interests include radio frequency microsystems and their applications for timing and signal processing.

Dr. Lu received the Best Student Paper Awards at the 2017 IEEE International Frequency Control Symposium and the 2018 IEEE International Ultrasonics Symposium, the 2015 Lam Graduate Award from the College of Engineering at UIUC, the 2017 Nick Holonyak, Jr. Graduate Research Award, the 2018 Nick Holonyak, Jr. Fellowship, and the 2019 Raj Mittra Outstanding Research Award from the Department of Electrical and Computer Engineering at UIUC.



Hongyan Zhou received the B.E. degree in inorganic nonmetallic materials engineering from the Changchun University of Science and Technology, Changchun, China, in 2017. She is currently pursuing the Ph.D. degree in microelectronics and solid state electronics at Chinese Academy of Sciences, Shanghai, China.

She joined the State Key Laboratory of Functional Materials for Informatics, Shanghai Institute of Microsystem and Information Technology, Chinese Academy of Sciences. Her research interests

include the design and microfabrication techniques of MEMS resonators, and filters.



Steffen Link (Student Member, IEEE) received the B.S. degree in computer engineering from the South Dakota School of Mines and Technology, Rapid City, SD, USA, in 2018. He is currently pursuing the master's degree at the University of Illinois at Urbana–Champaign, Urbana, IL, USA.

His research interests include design and microfabrication techniques of MEMS resonators, filters, and other radio frequency microsystems.



Yansong Yang (Member, IEEE) received the B.S. degree in electrical and electronic engineering from the Huazhong University of Science and Technology, Wuhan, China, in 2014, and M.S. and Ph.D. degrees in electrical engineering from the University of Illinois at Urbana–Champaign, Urbana, IL, USA, in 2017 and 2019, respectively.

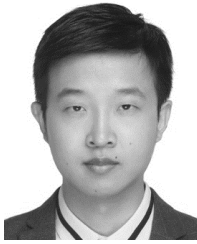
He is currently a Post-Doctoral Researcher with the University of Illinois at Urbana–Champaign. His research interests include design and microfabrication techniques of RF MEMS resonators, filters, switches, and photonic integrated circuits.

Dr. Yang has won the Second Place in Best Paper Competition at the 2018 IEEE International Microwave Symposium, and the Best Paper Award at the 2019 IEEE International Ultrasonics Symposium. He was also a recipient of the 2019 P. D. Coleman Graduate Research Award from the Department of Electrical and Computer Engineering at UIUC. He was a Finalist for the Best Paper Award at the 2018 IEEE International Frequency Control Symposium.



Zhongxu Li received the B.S. degree in materials science and engineering from Nanchang University, Nanchang, China, in 2017. He is currently pursuing M.S. and Ph.D. degrees in microelectronics and solid state electronics from the Shanghai Institute of Microsystems and Information Technology, University of Chinese Academy of Sciences, Shanghai, China.

His current research interests include the fabrication of wafer scale piezoelectric thin films mainly about lithium niobate and lithium tantalate; meanwhile, the design and microfabrication of surface acoustic wave device.



Kai Huang received the B.E. degree in microelectronics from Jilin University, Changchun, China, in 2013, and the Ph.D. degree in microelectronics and solid state electronics from the University of Chinese Academy of Sciences (CAS), Beijing, China, in 2018.

He is currently an Assistant Researcher with the Shanghai Institute of Microsystem and Information Technology, CAS. His current research interests include the research and development and mass production of piezo thin films on heterogeneous substrates.



Xin Ou received the Ph.D. degree in microelectronics and solid-state electronics from the Shanghai Institute of Microsystem and Information Technology (SIMIT), Chinese Academy of Sciences, Shanghai, China, in 2010.

He is currently a Professor with the State Key Laboratory of Functional Material for Informatics, SIMIT. He has authored more than 80 SCI papers and been authorized 14 patents. His current research interests include the heterointegration of functional materials for high-performance electrical, optical

and acoustical devices, especially, the piezoelectric hybrid substrate for 5G RF-filter application.

Dr. Ou was a recipient of the “IBMM Prize” of 20th International Conference on Ion Beam Modification of Materials, the “Young Investigator Award” of 18th International Conference on Ion Implantation Technology (IIT 2010), the “Research Prize” of Helmholtz Zentrum Dresden Rossendorf Germany, the Beijing “Science and Technology Progress Award” (first grade), the “2019 Ten Achievements of Optics” in China, the “Excellent Doctor Degree Dissertation Award” of the Chinese Academy of Sciences.



Songbin Gong (Senior Member, IEEE) received the Ph.D. degree in electrical engineering from the University of Virginia, Charlottesville, VA, USA, in 2010.

He is currently an Associate Professor and the Intel Alumni Fellow with the Department of Electrical and Computer Engineering and the Micro and Nanotechnology Laboratory, University of Illinois at Urbana–Champaign, Urbana, IL, USA. His research primarily focuses on design and implementation of radio frequency microsystems, components, and subsystems for reconfigurable RF front ends. In addition, his research explores hybrid microsystems based on the integration of MEMS devices with photonics or circuits for signal processing and sensing.

Dr. Gong was a recipient of the 2014 Defense Advanced Research Projects Agency Young Faculty Award, the 2017 NASA Early Career Faculty Award, and the 2019 UIUC College of Engineer Dean’s Award for Excellence in Research. Along with his students and postdocs, he received the Best Paper Awards from the 2017 and 2019 IEEE International Frequency Control Symposium, the 2018 International Ultrasonics Symposium, and won the Second Place in Best Paper Competition at the 2018 IEEE International Microwave Symposium. He is the Technical Committee Chair of MTT TC-6 Microwave Acoustics and RF-MEMS of the IEEE Microwave Theory and Techniques Society, and currently serves as an Associate Editor for T-UFFC and JMEMS.